ARTICLE

Check for updates

Controlling electromagnetic surface waves with conformal transformation optics

Xiaoyu Zhao [1,2], Hong Deng [1,2], Xiaoke Gao [1,2], Xikui Ma[1] & Tianyu Dong [1✉]

The application of transformation optics to the development of intriguing electromagnetic devices can produce weakly anisotropic or isotropic media with the assistance of quasi-conformal and/or conformal mapping, as opposed to the strongly anisotropic media produced by general mappings; however, it is typically limited to two-dimensional applications. By addressing the conformal mapping between two manifolds embedded in three-dimensional space, we demonstrate that electromagnetic surface waves can be controlled without introducing singularity and anisotropy into the device parameters. Using fruitful surface conformal parameterization methods, a near-perfect conformal mapping between smooth manifolds with arbitrary boundaries can be obtained. Illustrations of concealing and illusions, including surface Luneburg and Eaton lenses and black holes for surface waves, are provided. Our work brings the manipulation of surface waves at microwave and optical wavelengths one step closer.

[1] School of Electrical Engineering, Xi'an Jiaotong University, Xi'an 710049, China. [2]These authors contributed equally: Xiaoyu Zhao, Hong Deng, Xiaoke Gao.
✉email: tydong@mail.xjtu.edu.cn

Since its inception in the design of electromagnetic cloaks[1,2], transformation optics (TO) has proven to be a powerful tool to understand and customize the physics in acoustics[3], optics[4], mechanics[5], and thermodynamics[6,7], etc. Following the groundbreaking work of concealing objects, a number of other electromagnetic devices have been reported within the theoretical framework of TO, such as electromagnetic concentrators[8,9], field rotators[10], optical lenses[11,12], and optical illusion devices[13,14], to name a few. In practice, however, traditional TO often yields significant anisotropy in a designed medium[15]. Thus, metamaterials are often used to infer spatial changes from coordinate transformation geometry, which is based on the mathematical equivalence between geometry and material[16].

To reduce the anisotropy of the functional medium induced by TO, various approaches have been developed. By constructing mapping in non-Euclidean space, for example, it is possible to remove singular points formed by traditional TO[17], hence minimizing anisotropy. But for wavelengths comparable to the size of the transform region, non-Euclidean TO may perform even worse[18]; thus, several research projects focus on conformal or quasi-conformal mappings to achieve isotropy[19]. In $\mathbb{R}^2$, the concept of a carpet cloak that resembles a flat ground plane is successfully realized with an isotropic medium produced by minimizing the Modified-Liao functional under sliding boundary conditions[20], or equivalently by constructing the quasi-conformal mapping by solving the inverse Laplace equations[21]. Although the concept of carpet cloak has been extended to $\mathbb{R}^3$ by extrusion or revolution of a two-dimensional refractive index profile to control the reflection of free-space waves, it is only applicable to surfaces with translational or rotational symmetry[22].

Previous research has focused mainly on controlling propagating waves by TO, while less attention has been paid to the manipulation of surface waves[12,23,24]. Perfect surface wave concealing has been proposed by equating the optical path length of a ray traversing a flat plane with a homogeneous refractive index to the optical path on a curved surface with an angle-dependent refractive index for two orthogonal paths[25,26], which have been experimentally validated[27]. Although an electrically large object may be hidden by such a concealing device with an inhomogeneous isotropic medium, this approach is limited to rotationally symmetric surfaces. By linking the governing eikonal equations on a virtual flat plane and on a curved surface by transformation optics, the projection mapping yields surface wave concealing for non-rotationally symmetric geometries but with high anisotropy[14,28]. Considerable effort has been devoted to reducing such anisotropy by employing efficient numerical conformal algorithms such as boundary first flattening (BFF)[29], yet only surfaces with circular boundaries are investigated[30].

In this work, we show how to manipulate surface waves on smooth manifolds embedded in $\mathbb{R}^3$ within the framework of conformal TO, requiring an effective isotropic material under the regime of geometrical optics. Figure 1 illustrates a conformal surface mapping between two smooth manifolds in $\mathbb{R}^2$ and $\mathbb{R}^3$, i.e., $f : \mathcal{M}' \to \mathcal{M}$. The curved manifold $\mathcal{M}$ shown in Fig. 1a has been uv-parameterized and the mesh grid can be considered as the mapping result of the Cartesian coordinate system (x', y') in Fig. 1b. When the mapping is conformal or quasi-conformal, the face element dS remains right-angled, indicating that the elements are just scaled with little distortion. From the local coordinate systems on dS and dS' (see Supplementary Fig. 1a in Supplementary Note 1), one can derive the Jacobian matrix $\mathbf{J}$ of the mapping f with two singular values $\sigma_{J1} = \sigma_{J2} = \sigma_J$ that state equal scaling in two orthogonal directions[31]. Consequently, an isotropic concealing medium distribution $n = 1/\sqrt{\det(\mathbf{J})} = 1/\sigma_J$ can be obtained based on the conformal TO[19], representing the ratio of
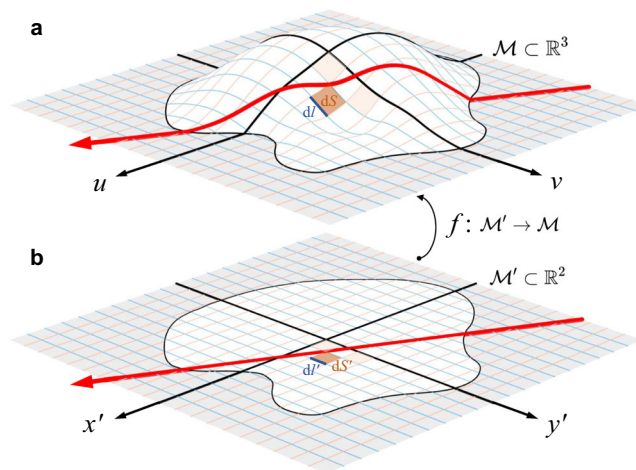

Fig. 1 The conformal mapping between manifolds. a A red light beam that crosses a curved two-dimensional manifold $\mathcal{M}$ embedded in $\mathbb{R}^3$. **b** A red light beam that crosses a flat two-dimensional manifold $\mathcal{M}'$ in $\mathbb{R}^2$. The manifold $\mathcal{M}$ is uv-parameterized, and both manifolds are plotted with a coordinate grid. The manifold $\mathcal{M}$ from $\mathcal{M}'$ can be obtained by using a certain analytic or numerical mapping $f : \mathcal{M}' \to \mathcal{M}$. The blue line element dl' and the brown face element dS' in $\mathcal{M}'$ are scaled to dl and dS in $\mathcal{M}$ after mapping f.

the line element dl' in the virtual space to the scaled element dl in the physical space to compensate for the length of the optical path[2]. As a result, light propagating on curved $\mathcal{M}$ behaves as light propagating on flat $\mathcal{M}'$. In practice, it is more convenient to describe mesh vertices in $\mathbb{R}^3$ in a Cartesian coordinate system $\{x, y, z\}$ and the Jacobian derived from the local coordinate system forms an asymmetric rank-two matrix $\mathbf{J}_{3 \times 2}$. In addition, possible quasi-conformal mappings can be measured by the conformality, i.e., the ratio $Q = \max(\sigma_{J1}/\sigma_{J2}, \sigma_{J2}/\sigma_{J1})$. A unity ratio Q allows an effective concealing medium expressed as $n_{\text{concealment}} = 1/\sqrt{\sigma_{J1}\sigma_{J2}}$ for all elements of the face[20].

Results

Surface electromagnetic wave concealment. Having obtained a conformal mapping between the manifolds $\mathcal{M} \in \mathbb{R}^3$ and $\mathcal{M}' \in \mathbb{R}^2$, we first design an isotropic surface wave concealing device from the perspective of conformal TO and compare its performance with the traditional surface wave concealment with anisotropic medium[14]. Simulations were carried out on a double-camelback bump (see Supplementary Note 2 for details) with an elliptical base profile embedded in $\mathbb{R}^3$, as shown in Fig. 2. Compared to scattering when the surface has no index profile (see Supplementary Fig. 2a in Supplementary Note 1), one can observe that the surface wave concealment is successfully achieved by two distinct approaches: one induced by the projection mapping proposed in[14] (Fig. 2a) and the other originates from the proposed quasi-conformal mapping (Fig. 2b). The corresponding material characteristics for the two types of concealing devices are displayed in Fig. 2c, indicating that the former is strongly anisotropic, while the latter is almost isotropic. In addition, the isotropic refractive index $n_{\text{c,double}}$ (the subscript "c" denotes the concealment, and "double" denotes the double-camelback bump) ranges from 0.83 to 1, which decreases as the bump height increases because a longer geometrical distance needs to be compensated by a smaller refractive index in order to attain equal optical path length. As references, simulation results of the concealment when the incident waves propagate along the y-axis and
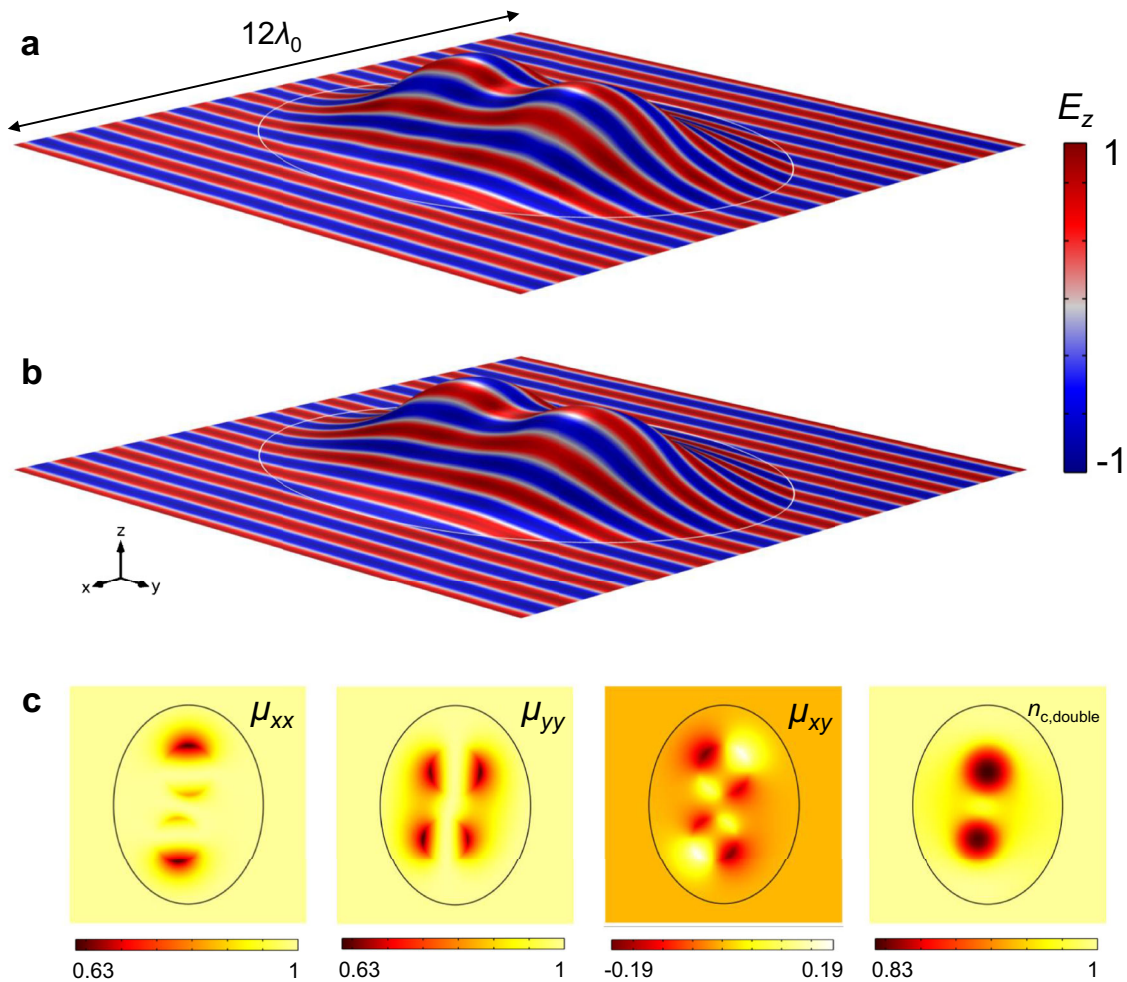
Fig. 2 The field and medium distribution for concealment. Normalized electric field distribution of surface electromagnetic wave concealing devices achieved by **a** anisotropic relative permeability and **b** isotropic refractive index. **c** Components of anisotropic relative permeability, μ_{xx}, μ_{yy}, and μ_{xy} and isotropic refractive index n. Excitation is a z-polarized plane wave with a magnitude of $|E_z| = 1$ V/m; and the wavelength in free space is $\lambda_0 = 20$ mm. The bump with a height of $1.25\lambda_0$ is located in the center of the square waveguide with a width of $12\lambda_0$. The white curves in **a** and **b** and the black curves in **c** depict the elliptical boundaries of double-camelback surfaces. The lengths of the semi-minor and semi-major axes are $a = 3.75\lambda_0$ and $b = 5\lambda_0$, respectively, along with the x- and y axes.

$45°$ from the x-axis (referred to as oblique incidence hereafter) are shown in Supplementary Fig. 3 in Supplementary Note 1.

The proposed scheme based on conformal TO has achieved near-perfect surface wave concealing while eliminating the anisotropy in the transformation medium that the traditional scheme presents. The distribution of $n_{c,double}$ in Fig. 2c outlines an asymmetric geometric profile, showing that the effectiveness of this scheme is independent of any symmetry. Such an achievement requires mappings with high conformality rather than those bringing large distortion such as the projection mapping[14]. The numerical method we adopt here[29] can obtain a quasi-conformal mapping with $Q < 1.03$, as shown in Supplementary Fig. 2b (see Supplementary Note 1), which is sufficient to design an effective isotropic concealing medium distribution.

Surface electromagnetic wave illusions. As the antithesis of concealment, optical illusion devices can reproduce the scattering characteristics of a specific object on other objects through a transformation medium[13,14]. Figure 3a depicts the surface electromagnetic wave scattered by a single-camelback bump $\mathcal{M}$ (see Supplementary Note 2 for details) filled with homogeneous material. Traditionally, if one wants to reproduce its scattering in a plane region $\mathcal{M}'$, the quasi-conformal mapping for designing

the illusion device is $f' : \mathcal{M} \rightarrow \mathcal{M}'$ with a Jacobian matrix $\mathbf{\Lambda}_{2 \times 3}$. Figure 3b shows the accurately recurring scattering characteristics in the plane region $\mathcal{M}'$ filled with $n_{i,plane} = 1/\sqrt{\sigma_{\Lambda 1}\sigma_{\Lambda 2}}$ (the subscript 'i' denotes the illusion, and 'plane' denotes the plane region), where $\sigma_{\Lambda 1}$ and $\sigma_{\Lambda 2}$ are singular values of $\mathbf{\Lambda}_{2 \times 3}$. Furthermore, Fig. 3c illustrates that the double-camelback bump filled with a carefully designed isotropic medium distribution can reproduce the same scattering pattern as shown in Fig. 3a. This illusion is realized by cascading two conformal mappings described in Supplementary Fig. 4 (see Supplementary Note 1), i.e., f_1 from $\mathbb{R}^3$ (virtual space) to $\mathbb{R}^2$ (intermediate space), and f_2 from $\mathbb{R}^2$ to $\mathbb{R}^3$ (physical space). Thus, the illusion medium for the double-camelback bump reads $n_{i,double} = n_{i,plane} \cdot n_{c,double}$. Figure 3d displays the profiles of $n_{i,plane}$ (for Fig. 3b) and $n_{i,double}$ (for Fig. 3c), respectively, which range from 1 to 1.25 ($n_{i,plane}$) and from 0.85 to 1.21 ($n_{i,double}$). The simulation results of the illusions for the oblique incidence and normal incidence along the y axis are provided in the Supplementary Note 1 (see Supplementary Fig. 5).

The scattering pattern of the single-camelback bump (Fig. 3a) has been successfully reproduced in the plane region (Fig. 3b) and on the double-camelback bump (Fig. 3c), which demonstrates that the proposed scheme is a general solution to illusion design
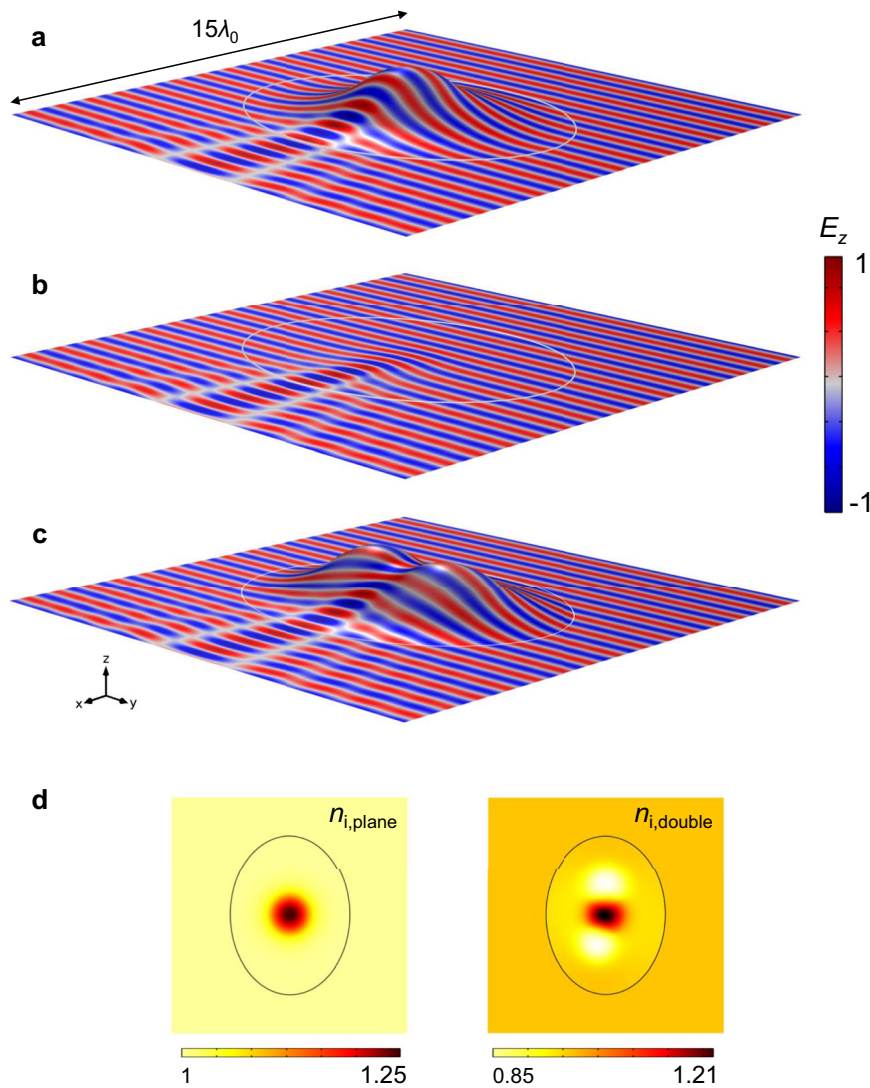
Fig. 3 Normalized electric field distribution of surface electromagnetic wave scattering. a Scattering on the single-camelback bump when filled with homogeneous medium. **b** Illusion of a single-camelback bump appearing in the plane. **c** Illusion of the single-camelback bump appearing on the double-camelback bump. **d** Isotropic refractive indices: $n_{i,plane}$ for the elliptic plane region and $n_{i,double}$ for the double-camelback bump. The bump with a height of $1.25\lambda_O$ is located in the center of the square waveguide with a width of $15\lambda_O$. The white curves in **a–c** and black curves in **d** depict the elliptical boundaries of the single-camelback surface, the plane region, and the double-camelback surface. The elliptical base profile is the same as that of Fig. 2.

on smooth two-dimensional manifolds. The cascading method to construct mappings between manifolds embedded in $\mathbb{R}^3$ can even tackle surfaces with different base profiles, since a conformal mapping between simply connected regions in $\mathbb{R}^2$ exists according to the Riemann mapping theorem[32]. Furthermore, the quasi-conformal ratios Q of the two mappings for the double-camelback and single-camelback bump are smaller than 1.03 (see Supplementary Fig. 2b in Supplementary Note 1) and 1.012 (see Supplementary Fig. 6c in Supplementary Note 1), respectively, implicating that the cascaded mapping meets the requirement for high conformality. The range of $n_{i,single}$ (1 to 1.25) (the subscript "single" denotes the single-camelback bump) is the inverse of that of the concealing refractive index $n_{c,single}$ (0.8 to 1) shown in Supplementary Fig. 6b in Supplementary Note 1, because the illusion can be regarded as the inverse design of concealing such that the Jacobian matrices of their corresponding mappings are the Moore-Penrose pseudoinverses of each other[31].

Surface wave Luneburg lens, Eaton lens, and black hole. Now that the wave behavior on the curved manifold can be

manipulated flexibly, it is natural to consider designing various complicated devices on it, such as surface wave Luneburg lens, Eaton lens, and black hole for surface waves[12,23,33,34]. Traditional designs are usually based on spherical or circular profiles with a constant radius. For an elliptical profile without a constant radius, we adopt the distance from the point on the ellipse to the center or the coordinate origin as the generalized radius, i.e., $R(\theta) = \sqrt{(a\cos\theta)^2 + (b\sin\theta)^2}$, where $\theta = \arctan(y/x)$ with (x, y) being the coordinates[35–37]. Thus, the refractive index of the considered Luneburg lens can be expressed as

$$n_L(r, \theta) = \sqrt{2 - \left(\frac{r}{R(\theta)}\right)^2},\qquad(1)$$

where $r = \sqrt{x^2 + y^2}$. Similar to the traditional circular Luneburg lens, this distribution retains $n_L = 1$ (the subscript "L" denotes the Luneburg lens) on the boundary and $n_L = \sqrt{2}$ in the center $r = 0$[38]. Next, the medium distribution of a Luneburg lens on the double-camelback bump can be expressed as $n_{Luneburg} = n_{c,double} \cdot n_L$. As illustrated in Fig. 4a, two Gaussian beams with a
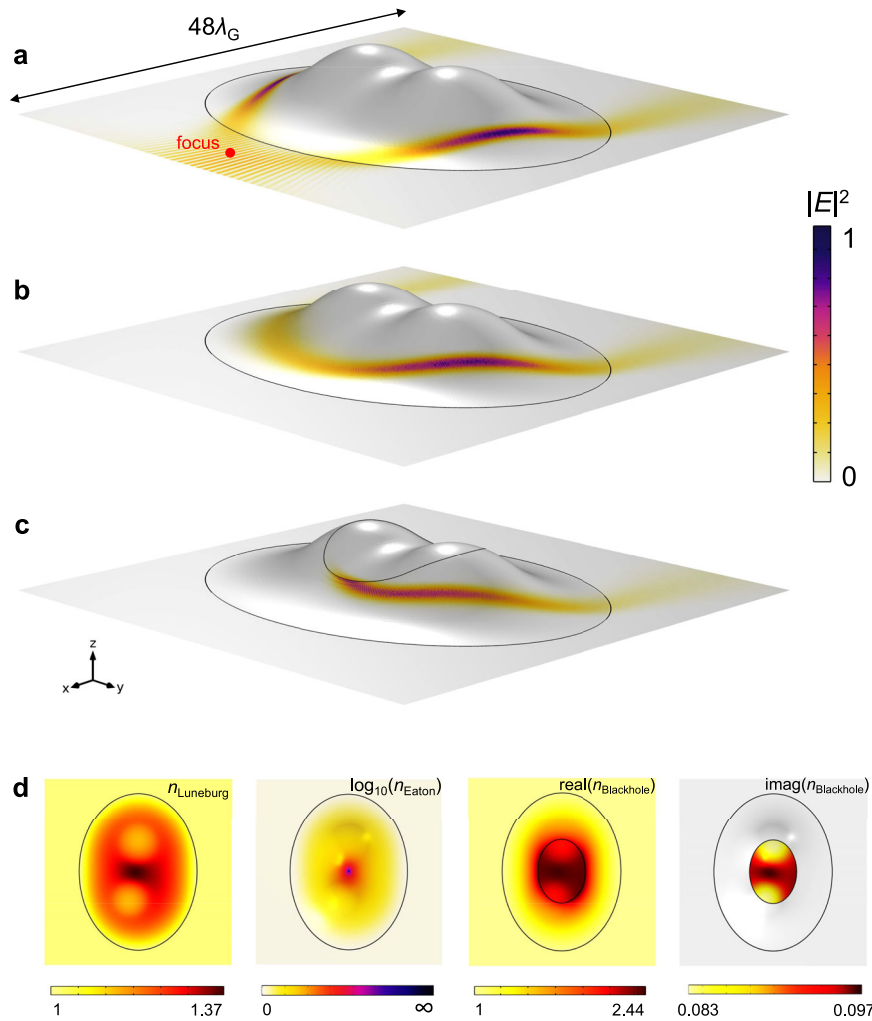
Fig. 4 Normalized electric field distribution on surface electromagnetic wave devices. Gaussian beam is applied to demonstrate their functions. **a** The Luneburg lens, **b** the Eaton lens, and **c** the black hole on the double-camelback surface are designed by covering the concealment with a medium of devices. **d** Isotropic refractive indices: $n_{Luneburg}$ for the Luneburg lens, the decimal logarithm of n_{Eaton} for the Eaton lens, and the real and imaginary parts of $n_{Blackhole}$ for the black hole. The bump with a height of $5\lambda_G$ is located in the center of the square waveguide with a width of $48\lambda_G$. The black curves in **a**–**d** depict the boundaries of double-camelback surfaces and the inner core of the black hole. The lengths of the semi-minor and semi-major axes of the elliptical base profile are $a = 15\lambda_G$ and $b = 20\lambda_G$, respectively, along with the x and y axes. The red focal point of the Luneburg lens is located at a distance of $20\lambda_G$ from the center.

free-space wavelength $\lambda_G = 50$ mm (the subscript "G" denotes the Gaussian beam) and waist radius $w_0 = \lambda_G$ are incident along the x-direction at the position $\pm 0.8b$ in the y direction and reflected by the Luneburg lens to interfere at the focus point. The focal distance reads $20\lambda_G$, which is identical to the unit circular Luneburg lens. For the Eaton lens, the refractive index n_E (the subscript "E" denotes the Eaton lens) reads as

$$n_E(r, \theta) = \sqrt{2R(\theta)/r - 1}, \qquad (2)$$

which can approach infinity when $r = 0$, leaving a singular point to be cared for. Figure 4b describes that a Gaussian beam that goes along the x-direction bends to the inverse x-direction after passing through the Eaton lens on the double-camelback bump. The proposed surface wave Luneburg and Eaton lenses may be deployed in optical imaging, signal acquisition, and novel designs for surface wave microwave antennas. Another functional device that can rotate beam propagation is the peripheral of the two-layer optical black hole, where light is compelled to travel in a spiral path into the absorbing medium at the core. The piece-wise refractive index distribution function n_B (the subscript "B"

denotes the black hole) can be expressed as

$$n_B(r, \theta) = \begin{cases} 1, & r > R(\theta) \\ R(\theta)/r, & r_{core} \cdot R(\theta) < r < R(\theta) \\ 1/r_{core} + i\gamma, & r < r_{core} \cdot R(\theta) \end{cases} \qquad (3)$$

where $r_{core} = 0.4$ is the scaling factor of the internal ellipse core compared with the base profile and $\gamma = 0.1$ is the loss factor. The refractive index distribution $n_{Blackhole} = n_{c,double} \cdot n_B$ on the double-camelback bump is depicted in Fig. 4d. The real part of the material parameters is matched on the inner boundary, and the imaginary part for absorbing energy ranging from 0.083 to 0.097 exists only in the core. The same Gaussian beam used for the Eaton lens is employed, and the result in Fig. 4c shows that the beam bends around 90° before it reaches the inner boundary and is absorbed by the lossy core without reflection, showing potential application in interference reduction and energy harvesting for electronic devices. As references, simulation results of the lenses when waves are incident along the y axis direction and 45° from x axis direction are illustrated in Supplementary Fig. 7 in Supplementary Note 1. Note that the overall sizes of the

simulation models are larger than ten times the operating wavelength, demonstrating that the proposed scheme is capable of managing surface wave behaviors on electrically large objects. Moreover, the excellent performance of these functional surface wave devices demonstrates that, based on the proposed scheme, a variety of novel devices may be realized on smooth curved manifolds, which may facilitate the development of miniaturized and integrated photonic devices.

Discussion

Our theory and method are based on geometrical optics. It requires small curvature and little variation in wavelength (see Eqs. (7) and (8) in Methods), which can be expressed as

$$w = |\nabla\lambda| = |\nabla(\lambda_0/n)| = \lambda_0|\nabla n|/n^2 \ll 1, \quad (4)$$

$$\rho = |R_{ij}|\lambda^2 = |Kg_{ij}|(\lambda_0/n)^2 = \det(g_{ij})K^2\lambda_0^2/n^2 = K^2\lambda_0^2/n^6 \ll 1, \quad (5)$$

where R_{ij} is the Ricci curvature tensor, K is the Gaussian curvature, and g_{ij} is the metric tensor. Both the wavelength index w and the curvature index ρ are inversely proportional to the powers of the refractive index n. To prevent w and ρ from drastically increasing, a height lower than half of the base radius is favorable, and thereby the optical path length can be compensated for with a nearly uniform refractive index. On this basis, requirements Eqs. (4) and (5) demand a shorter wavelength λ_0 and a smoother geometric structure to ease the change rate $|\nabla n|$ and the Gaussian curvature K. As a negative example, a hemisphere surface wave concealment is reviewed and results are displayed in Supplementary Fig. 8 in Supplementary Note 1, whose refractive index $n_{c,sphere}$ is between 0.5 and 1 (see Supplementary Fig. 8d) and the maximum of quasi-conformal ratio Q is smaller than 1.012 (see Supplementary Fig. 8e). The visible scattering $E_z - E_{bz}$ (the subscript "b" denotes the background field) appearing in the plane in Supplementary Fig. 8c demonstrates the failure of geometrical optics due to the high curvature index $\rho > 20$ residing in the right-angle connection between the hemisphere and the plane, as shown in Supplementary Fig. 8f, and the average curvature index $\bar{\rho} = 1.57$ is also higher than 1. The non-smooth connection causes the phase distortion in the backward scattering (see Supplementary Note 3 for the details), and the maximum of the forward scattering $|E_z - E_{bz}|_{max} = 0.75 \,\text{V/m}$ implies a phase difference $\arcsin(0.75) = 48.6°$ resulted from the reconstruction of wave fronts. In comparison, Supplementary Fig. 2c and Supplementary Fig. 6d display the average curvature index $\bar{\rho} = 0.54$ for double-camelback bump and $\bar{\rho} = 0.39$ for single-camelback bump, respectively, both satisfying the requirement Eq. (5) and leaving near-zero ρ on smooth boundaries. It may be noticed that the wavelength index w for the concealing devices shown in Supplementary Fig. 2d, Supplementary Fig. 6e, and Supplementary Fig. 8g is smaller than unity everywhere because it is related to lower powers of λ_0 and n; thus, it is much easier to meet the requirement of Eq. (4) compared to Eq. (5). These selected curvature and wavelength characteristics that validate the approximation of geometrical optics are indispensable for the excellent performance of electromagnetic devices.

The isotropic case that determines the expression of requirements Eqs. (4) and (5) is based on the conformal or quasi-conformal mappings between two-dimensional manifolds. Benefiting from the rapid development in conformal parameterization, a series of mapping methods can be used to design surface wave concealment[29,39,40]. The BFF method[29] adopted in our study can establish near-perfect conformal mappings not only between smooth manifolds but also surfaces with cuspidal points, such as sharp corners and cone singularities, offering exhilarating promise for wave manipulation on more complicated surfaces. In addition, there are algorithms aimed at constructing quasi-conformal mappings

between high-genus manifolds[41,42], which can be used to deal with phase regulation on surfaces with holes. One noteworthy idea is to map a high-genus surface to a zero-genus plane region by transforming holes into slits[43,44] which implies the possibility for the scheme conducted in simply connected regions to manipulate wave behaviors on multiple connected surfaces. In addition, it should be pointed out that high conformality of the mapping always relies on the surface parameterization algorithms and intrinsic curing degree of geometries (see Supplementary Note 4 for a detailed discussion). By reasonably utilizing advanced algorithms for a variety of particular cases, our method has the potential to be a universal scheme for controlling surface electromagnetic waves on an arbitrary two-dimensional manifold.

Conclusions

In summary, we have proposed a general method to manipulate electromagnetic waves on smooth two-dimensional manifolds without rotational symmetry by means of a certain isotropic refractive index distribution derived from the quasi-conformal mapping. The relationship between medium and mappings is induced from the wave equation on the manifold under the geometrical optics approximation. Numerical quasi-conformal algorithms are introduced to construct mappings between manifolds, and consequent functional mediums are validated by concealing surfaces and generating illusions on plane regions. By cascading mappings between $\mathbb{R}^2$ and $\mathbb{R}^3$ to obtain a mapping between $\mathbb{R}^3$, we succeed in reproducing the scattering of a surface on another surface. In addition, functional devices such as surface Luneburg lenses, surface Eaton lenses, and black holes for surface waves are designed based on carpet cloaks. Finally, the indices required by geometrical optics are reviewed to demonstrate the validity of the approximation on simulation models. Our method paves the way for the regulation of surface electromagnetic waves on any two-dimensional manifold and can be utilized to control surface waves in other fields, such as acoustics, mechanics, and thermodynamics.

Methods

Conformal transformation optics for surface waves

Wave equation on curved manifold. The concept of transformation medium comes from the equivalence between geometry and media. Within the Einstein summation convention, Maxwell's wave equation for the electric field $\nabla_{\mathcal{M}} \times \nabla_{\mathcal{M}} \times \mathbf{E} - \mu_0\varepsilon_0\partial_t^2\mathbf{E} = 0$ in free space can be expressed as ref. [16]

$$\nabla^j\nabla_j E_i - R_{ij}E^j - c_0^{-2}\partial_t^2 E_i = 0, \quad (6)$$

where $c_0 = 1/\sqrt{\mu_0\varepsilon_0}$ is the light velocity in free space; R_{ij} is the Ricci tensor of the considered geometry $\mathcal{M}$. Supposing that electromagnetic waves are confined near a curved surface $\mathcal{M}$ embedded in $\mathbb{R}^3$ as surface waves, its local plane wave solution reads $E_i = \mathscr{E}_i \exp(i\varphi)$ with constant complex amplitudes $\mathscr{E}_i$, where the phase reads $\varphi = \mathbf{k} \cdot \mathbf{r} - \omega t$ with the wave vector $\mathbf{k} = \nabla_{\mathcal{M}}\varphi$ and angular frequency $\omega = -\partial_t\varphi$. For surface waves, the wave vector $\mathbf{k}$ lies in the tangent space of the curved surface $\mathcal{M}$, i.e., $\mathbf{k} \in \mathcal{T}(\mathcal{M})$. Thus, Eq. (6) can be simplified and approximated in the regime of geometrical optics where the wavelength $\lambda = 2\pi/k$ varies slowly with distance, i.e.,

$$|\nabla_{\mathcal{M}}\lambda| \ll 1. \quad (7)$$

In addition, the effective curvature of the curved surface should be small enough compared to the wavelength so that the assumption of locally plane waves is valid, i.e.,

$$|R_{ij}|\lambda^2 \ll 1. \quad (8)$$

As a result, inserting $E_i = \mathscr{E}_i \exp(i\varphi)$ into Eq. (6) and considering that the (spatial and temporal) derivatives of $\mathscr{E}_i$ vanish, one can obtain the dispersion relation for the surface wave propagating on $\mathcal{M}$, which reads as

$$k^2 = k^j k_j = g^{ij}k_i k_j = \omega^2/c_0^2. \quad (9)$$

Here, g_{ij} is the induced metric tensor for the curved surface $\mathcal{M}$, which can be determined from the transformation of the Jacobian matrix from the manifold $\mathcal{M}'$ in $\mathbb{R}^2$ to $\mathcal{M}$[31].

Wave equation on a flat plane. Alternatively, if $\mathcal{M}$ is flat (i.e., $R_{ij} = 0$) and filled with anisotropic medium denoted by relative permeability tensor μ^{ij}, Eq. (6) becomes

$$\nabla \times (\boldsymbol{\mu}^{-1} \cdot \nabla \times \mathbf{E}) - \mu_0 \varepsilon_0 \partial_t^2 \mathbf{E} = 0. \tag{10}$$

Suppose that the electromagnetic waves are confined near $\mathcal{M}$ and the electric field $\mathbf{E}$ is perpendicularly polarized. In a Cartesian coordinate system, if $\mathcal{M}$ can be placed in the xy plane, we focus on the case that the electric field vector $\mathbf{E}$ lies in the normal space of the flat plane $\mathcal{M}$, i.e., $\mathbf{E} \in \mathcal{N}(\mathcal{M})$, and the global wave solution may read $E_z = \mathscr{E}_z \exp(i\varphi)$. Thus, the phase φ is independent of z and the wave vector lies on the plane as $\mathbf{k} = (k_x, k_y, 0)$, because a flat plane coincides with its tangent space. Since the flat manifold $\mathcal{M}$ has a zero curvature tensor, the condition Eq. (8) holds naturally. Once the other condition Eq. (7) is satisfied that the wavelength varies slowly, one may disregard the derivatives of the complex amplitude after inserting $E_z = \mathscr{E}_z \exp(i\varphi)$ into Eq. (10) and obtain the dispersion relation for the surface wave propagating on $\mathcal{M}$, which reads $(\mu_{xx} k_x^2 + 2\mu_{xy} k_x k_y + \mu_{yy} k_y^2)/\det(\boldsymbol{\mu}) = \omega^2/c_0^2$. By excluding consideration of the particular polarization, the dispersion equation can be recast within the Einstein summation convention as

$$\frac{1}{\det(\boldsymbol{\mu})} \mu^{ij} k_i k_j = \frac{\omega^2}{c_0^2}. \tag{11}$$

Transformation medium and geometry. For electromagnetic waves that behave identically on two manifolds, one can obtain the equivalence between geometry and material properties by comparing Eqs. (9) and (11), which yields

$$\frac{\mu^{ij}}{\det(\boldsymbol{\mu})} = g^{ij}. \tag{12}$$

The relative permeability tensor μ^{ij} actually creates an illusion in the flat plane because a spatial point filled with medium $\boldsymbol{\mu}$ is equivalent to a metric $\mathbf{g} = \det(\boldsymbol{\mu})\boldsymbol{\mu}^{-1}$. If the local Cartesian coordinate system at this point is aligned along the orthogonal eigenvectors of $\boldsymbol{\mu}$, the real and symmetric permeability tensor reduces to $\mathrm{diag}(\mu_x, \mu_y, \mu_z)$ so that the square of the line element in the direction x is $\mathrm{d}s^2 = g_{xx}\mathrm{d}x^2 = \mu_y \mu_z \mathrm{d}x^2$, which is also the square of the optical path length in the curved free space. Compared to $\mathrm{d}s^2 = n_x^2 \mathrm{d}x^2$ in the flat manifold, one can derive $n_x^2 = \mu_y \mu_z$ and similar results in the y and z directions. Consequently, the relationship between the relative permeability tensor $\boldsymbol{\mu}$ and the refractive index tensor $\mathbf{n}$ may be expressed as $\mathbf{n}^2 = \det(\boldsymbol{\mu})\boldsymbol{\mu}^{-1}$ and one may further obtain

$$\mathbf{n}_{\text{illusion}}^2 = \mathbf{g}, \tag{13}$$

by referring to Eq. (12). In a similar manner, the transformation medium can be obtained for H_z polarization. We stress that the proposed design method is polarization-independent (see Supplementary Note 5 for details).

Surface transformation and TO medium. The metric tensor in equation Eq. (13) is induced by the mapping $f: \mathcal{M}' \to \mathcal{M}$ and can be constructed by the Jacobian matrix $\mathbf{J}_{3 \times 2}$ as $\mathbf{g} = \mathbf{J}^{\mathrm{T}}\mathbf{J}$[31]. Nevertheless, we prefer to associate $\mathbf{n}_{\text{illusion}}$ with the Jacobian matrix $\boldsymbol{\Lambda}_{2 \times 3}$ that represents the transformation from $\mathbb{R}^3$ (virtual space) to $\mathbb{R}^2$ (physical space). Actually, the asymmetric Jacobian matrices $\mathbf{J}_{3 \times 2}$ and $\boldsymbol{\Lambda}_{2 \times 3}$ can be denoted as the Moore-Penrose pseudoinverse of each other[31], i.e., $\mathbf{J} = \boldsymbol{\Lambda}^{\dagger}$, where the superscript '†' denotes the pseudoinverse. Thus, one can rewrite the equivalence Eq. (13) as

$$\mathbf{n}_{\text{illusion}}^2 = \mathbf{g} = \mathbf{J}^{\mathrm{T}}\mathbf{J} = \left(\boldsymbol{\Lambda}\boldsymbol{\Lambda}^{\mathrm{T}}\right)^{-1}. \tag{14}$$

Similar relationship can be obtained for concealing medium $\mathbf{n}_{\text{concealment}}$ and corresponding Jacobian matrix $\mathbf{J}_{3 \times 2}$ from $\mathbb{R}^2$ (virtual space) to $\mathbb{R}^3$ (physical space) as

$$\mathbf{n}_{\text{concealment}}^2 = \left(\mathbf{J}^{\mathrm{T}}\mathbf{J}\right)^{-1}. \tag{15}$$

For the mapping between $\mathbb{R}^3$ (Supplementary Fig. 4), which is formed by cascading two transformations between $\mathbb{R}^3$ and $\mathbb{R}^2$, the consequent medium for the illusion can be recast as the combination of the concealing and illusion refractive index tensors, i.e.,

$$\mathbf{n}_{\text{illusion}}^2 = \left(\boldsymbol{\Lambda}_1 \boldsymbol{\Lambda}_1^{\mathrm{T}}\right)^{-1} \cdot \left(\mathbf{J}_2^{\mathrm{T}} \mathbf{J}_2\right)^{-1}, \tag{16}$$

where $\boldsymbol{\Lambda}_1$ and $\mathbf{J}_2$ are Jacobian matrices for mappings f_1 and f_2, as illustrated in Supplementary Fig. 4, respectively. In particular, when the mappings are conformal, the refractive index becomes isotropic and the corresponding Jacobian matrix has two identical singular values. Taking the determinants of Eqs. (14) and (15), the refractive indices can be denoted by singular values of the Jacobian matrices as $n_{\text{concealment}} = 1/\sigma_J$ and $n_{\text{illusion}} = 1/\sigma_\Lambda$.

Discrete conformal mapping and transformation medium

Review on discrete conformal mapping. It has been demonstrated that an isotropic refractive index distribution can be achieved by solving equations for equal optical path length only on rotationally symmetric surfaces[25]. Regarding the non-rotationally symmetric concealing device, high anisotropy is introduced by the projection mapping that distorts the coordinate grid[14]. However, numerical

algorithms for surface parameterization provide possible conformal mappings for arbitrary surfaces. For example, the angle-based flattening method[45,46] has been proposed to construct conformal parameterization by minimizing a punishing functional to decrease angular distortion, while its non-linearity reduces computational efficiency. In addition, the so-called least squares method[47] and the spectral method[48] have been introduced to achieve higher efficiency, benefiting from their linearity. Their disadvantages are free target boundaries and non-bijectivity, whereas we expect a one-to-one mapping that includes every point in physical and virtual space with controlled boundaries. Further research, such as disk conformal mapping[40], has been reported as a linear and bijective conformal mapping method but with a fixed disk boundary. Not until BFF[29] enabled editing of the boundary as demand was the drawbacks totally eliminated. To deal with a certain electromagnetic circumstance, an appropriate algorithm could be chosen from the preceding techniques[49,50].

Triangulation and Jacobian matrices. Supposing that the conformal mapping reads $f_1: \mathcal{M}_2 \to \mathcal{M}_1$ (or $f_2: \mathcal{M}_1 \to \mathcal{M}_2$) between manifolds $\mathcal{M}_1 \subset \mathbb{R}^3$ and $\mathcal{M}_2 \subset \mathbb{R}^2$, as shown in Supplementary Fig. 1a, one can find that a simplex $\mathcal{S}_1$ in meshed $\mathcal{M}_1$ and its counterpart in meshed $\mathcal{M}_2$ are a pair of similar triangles, which allows $\mathcal{S}_1$ and $\mathcal{S}_2$ to share a same barycentric coordinate system. This local coordinate system, as shown in Supplementary Fig. 1b, can represent any point inside the simplex as the linear combination of three vertices and helps quickly induce the Jacobian matrix of numerical mappings based on triangular mesh parameterization. For example, the location of the point $\mathbf{q}(x', y')$ on $\mathcal{S}_2$ can be expressed as $x' = \sum_{i=1}^{3} \lambda_i x_i'$ and $y' = \sum_{i=1}^{3} \lambda_i y_i'$ with $\lambda_1 + \lambda_2 + \lambda_3 = 1$, i.e., a linear combination of vertices $\mathbf{q}_1(x_1', y_1')$, $\mathbf{q}_2(x_2', y_2')$ and $\mathbf{q}_3(x_3', y_3')$. For the triangulation mesh, we can obtain the barycentric coordinates, which read as

$$\lambda_1 = \left[(y_2' - y_3')(x' - x_3') + (x_3' - x_2')(y' - y_3')\right]/\det(\mathbf{M}), \tag{17}$$

$$\lambda_2 = \left[(y_3' - y_1')(x' - x_3') + (x_1' - x_3')(y' - y_3')\right]/\det(\mathbf{M}), \tag{18}$$

$$\lambda_3 = \left[(y_1' - y_2')(x' - x_2') + (x_2' - x_1')(y' - y_2')\right]/\det(\mathbf{M}), \tag{19}$$

where $\det(\mathbf{M}) = \det([\mathbf{q}_1 - \mathbf{q}_3, \mathbf{q}_2 - \mathbf{q}_3]) = (x_1' - x_3')(y_2' - y_3') + (x_3' - x_2')(y_1' - y_3')$, with $\mathbf{q}_i(x_i', y_i')$ being the i-th vertices ($i = 1, 2, 3$). Here, Eqs. (17), (18), and (19) show that the barycentric coordinate system $(\lambda_1, \lambda_2, \lambda_3)$ can be expressed by the Cartesian coordinate system (x', y'). Regarding the point $\mathbf{p}(x, y, z)$ on $\mathcal{S}_1 \subset \mathbb{R}^3$, mapped from the point $\mathbf{q}$ in $\mathbb{R}^2$, we have $x = \sum_{i=1}^{3} \lambda_i x_i$, $y = \sum_{i=1}^{3} \lambda_i y_i$ and $z = \sum_{i=1}^{3} \lambda_i z_i$ as the linear combination of $\mathbf{p}_1(x_1, y_1, z_1)$, $\mathbf{p}_2(x_2, y_2, z_2)$ and $\mathbf{p}_3(x_3, y_3, z_3)$, since $\mathcal{S}_1$ and $\mathcal{S}_2$ share the same barycentric coordinates λ_i. As a result, the Jacobian matrix $\mathbf{J}_{3 \times 2}$ of the mapping from $\mathcal{S}_2 \subset \mathbb{R}^2$ to $\mathcal{S}_1 \subset \mathbb{R}^3$ can be derived according to the derivatives of $(\lambda_1, \lambda_2, \lambda_3)$ with respect to (x', y'), which reads as

$$\mathbf{J}_{3 \times 2} = \begin{pmatrix} \partial_{x'}x & \partial_{y'}x \\ \partial_{x'}y & \partial_{y'}y \\ \partial_{x'}z & \partial_{y'}z \end{pmatrix} = \frac{1}{\det(\mathbf{M})} \begin{pmatrix} x_1 & x_2 & x_3 \\ y_1 & y_2 & y_3 \\ z_1 & z_2 & z_3 \end{pmatrix} \begin{pmatrix} y_2' - y_3' & x_3' - x_2' \\ y_3' - y_1' & x_1' - x_3' \\ y_1' - y_2' & x_2' - x_1' \end{pmatrix}. \tag{20}$$

Similarly, one can derive the Jacobian matrix $\boldsymbol{\Lambda}_{2 \times 3}$ of the numerical mapping from $\mathcal{S}_1$ to $\mathcal{S}_2$; alternatively, one can calculate the Moore-Penrose pseudoinverse as $\boldsymbol{\Lambda}_{2 \times 3}$[31]. By calculating the Jacobian matrices $\mathbf{J}_{3 \times 2}$ or $\boldsymbol{\Lambda}_{2 \times 3}$ on each simplex, the information on the mapping f_1 or f_2 can be fully described.

Simulation methods

The wave behavior of electromagnetic devices is simulated using the finite element method. The geometric model is an optical thin film waveguide whose thickness is less than one-fifth of the wavelength. On the outer surfaces of the waveguide, the perfect electric conductor boundary condition is applied to emulate the propagation of the surface wave on a two-dimensional manifold. Thus, the propagation of the plane wave or Gaussian beam is restricted within the optical thin film. To mimic an open and non-reflecting infinite domain, perfectly matched layers are applied on the boundary of the propagating plane. The designed medium is configured to the waveguide as a fitting function interpolated from the discrete data set calculated on extra-dense meshes.

Data availability

All data needed to evaluate the conclusions in the paper are presented in the paper and/or the Supplementary Materials. Raw data and corresponding simulation data are available upon reasonable request.

Code availability

The code developed in this study is available from the authors upon reasonable request.

References

1. Pendry, J. B., Schurig, D. & Smith, D. R. Controlling electromagnetic fields. *Science* **312**, 1780–1782 (2006).
2. Leonhardt, U. Optical conformal mapping. *Science* **312**, 1777–1780 (2006).
3. Chen, H. & Chan, C. Acoustic cloaking in three dimensions using acoustic metamaterials. *Appl. Phys. Lett.* **91**, 183518–183518 (2007).
4. Wang, X. et al. Self-focusing and the talbot effect in conformal transformation optics. *Phys. Rev. Lett.* **119**, 033902 (2017).
5. Genov, D., Zhang, S. & Zhang, X. Mimicking celestial mechanics in metamaterials. *Nat. Phys.* **5**, 687–692 (2009).
6. Guenneau, S., Amra, C. & Veynante, D. Transformation thermodynamics: cloaking and concentrating heat flux. *Opt. Express* **20**, 8207–8218 (2012).
7. Raza, M., Liu, Y., Lee, E. & Ma, Y. Transformation thermodynamics and heat cloaking: a review. *J. Opt.* **18**, 044002 (2016).
8. Rahm, M. et al. Design of electromagnetic cloaks and concentrators using form-invariant coordinate transformations of maxwell's equations. *Photon. Nanostruct. Fundam. Appl.* **6**, 87–95 (2008).
9. Sadeghi, M. M., Li, S., Xu, L., Hou, B. & Chen, H. Transformation optics with Fabry-Pérot resonances. *Sci. Rep.* **5**, 1–7 (2015).
10. Luo, Y., Chen, H., Zhang, J., Ran, L. & Kong, J. A. Design and analytical full-wave validation of the invisibility cloaks, concentrators, and field rotators created with a general class of transformations. *Phys. Rev. B* **77**, 125127 (2008).
11. Perczel, J. & Leonhardt, U. Partial transmutation of singularities in optical instruments. *N. J. Phys.* **13**, 1005–1008 (2008).
12. Liu, Y., Zentgraf, T., Bartal, G. & Zhang, X. Transformational plasmon optics. *Nano Lett.* **10**, 1991–7 (2010).
13. Lai, Y. et al. Illusion optics: the optical transformation of an object into another object. *Phys. Rev. Lett.* **102**, 253902 (2009).
14. McManus, T., Valiente Kroon, J., Horsley, S. & Hao, Y. Illusions and cloaks for surface waves. *Sci. Rep.* **4**, 5977 (2014).
15. Schurig, D. et al. Metamaterial electromagnetic cloak at microwave frequencies. *Science* **314**, 977–980 (2006).
16. Leonhardt, U. & Philbin, T. Geometry and light: the science of invisibility. *2013 Conf. Lasers Electro-Opt. Eur. - Int. Quantum Electron. Conf.* (2013).
17. Leonhardt, U. & Tyc, T. Broadband invisibility by non-Euclidean cloaking. *Science* **323**, 110–112 (2009).
18. Tyc, T., Chen, H., Chan, C. T. & Leonhardt, U. Non-Euclidean cloaking for light waves. *IEEE J. Sel. Top. Quantum Electron.* **16**, 418–426 (2010).
19. Xu, L. & Chen, H. Conformal transformation optics. *Nat. Photonics* **9**, 15–23 (2015).
20. Li, J. & Pendry, J. B. Hiding under the carpet: a new strategy for cloaking. *Phys. Rev. Lett.* **101**, 203901 (2008).
21. Zheng, C., Zhou, X., Hu, J. & Hu, G. Design method for quasi-isotropic transformation materials based on inverse Laplace's equation with sliding boundaries. *Opt. Express* **18**, 6089–6096 (2010).
22. Landy, N., Kundtz, N. & Smith, D. Designing three-dimensional transformation optical media using quasiconformal coordinate transformations. *Phys. Rev. Lett.* **105**, 193902 (2010).
23. Zentgraf, T., Liu, Y., Mikkelsen, M., Valentine, J. & Zhang, X. Plasmonic luneburg and eaton lenses. *Nat. Nanotechnol.* **6**, 151–5 (2011).
24. Vakil, A. & Engheta, N. Transformation optics using graphene. *Science* **332**, 1291–4 (2011).
25. Mitchell Thomas, R. C., McManus, T. M., Quevedo-Teruel, O., Horsley, S. A. R. & Hao, Y. Perfect surface waves cloaks. *Phys. Rev. Lett.* **111**, 213901 (2013).
26. Mitchell Thomas, R., Quevedo Teruel, O., Sambles, J. & Hibbins, A. Omnidirectional surface wave cloak using an isotropic homogeneous dielectric coating. *Sci. Rep.* **6**, 30984 (2016).
27. La Spada, L. et al. Surface wave cloak from graded refractive index nanocomposites. *Sci. Rep.* **6**, 29363 (2016).
28. McManus, T. M., Spada, L. L. & Hao, Y. Isotropic and anisotropic surface wave cloaking techniques. *J. Opt.* **18**, 044005 (2016).
29. Sawhney, R. & Crane, K. Boundary first flattening. *ACM Trans. Graph.* **37**, 1–14 (2017).
30. Xu, L., Ge, H., Li, J., He, R. & Chen, H. Conformal landscape of a two-dimensional gradient refractive-index profile for geometrical optics. *Phys. Rev. Appl.* **13**, 054007 (2020).
31. Hormann, K., Levy, B. & Sheffer, A. Mesh parameterization: theory and practice. *ACM SIGGRAPH. Int. Conf. Comput. Graph. Interact. Techn.* **12**, 1–87 (2008).
32. Floater, M. & Hormann, K. Advances in multiresolution for geometric modelling (Springer Berlin Heidelberg, 2005).
33. Narimanov, E. & Kildishev, A. Optical black hole: broadband omnidirectional light absorber. *Appl. Phys. Lett.* **95**, 041106 (2009).
34. Dockrey, J. A. et al. Thin metamaterial luneburg lens for surface waves. *Phys. Rev. B* **87**, 125137 (2013).
35. Grzesik, J. A. Focusing properties of a three-parameter class of oblate, luneburg-like inhomogeneous lenses. *J. Electromagn.* **19**, 1005–1019 (2005).
36. Demetriadou, A. & Hao, Y. Slim luneburg lens for antenna applications. *Opt. Express* **19**, 19925–19934 (2011).
37. Gómez Correa, J., Coello, V., Garza Rivera, A., Puente, P. & Chávez-Cerda, S. Three-dimensional ray tracing in spherical and elliptical generalized luneburg lenses for application in the human eye lens. *Appl. Opt.* **55**, 2002 (2016).
38. Luneburg, R., Wolf, E. & Herzberger, M. Mathematical theory of optics (University of California, 1964).
39. Springborn, B., Schröder, P. & Pinkall, U. Conformal equivalence of triangle meshes. *ACM Trans. Graph.* **27**, 1–11 (2008).
40. Choi, P. T. & Lui, L. M. Fast disk conformal parameterization of simply-connected open surfaces. *J. Sci. Comput.* **65**, 1065–1090 (2015).
41. Zhang, M., Li, Y., Zeng, W. & Gu, X. Canonical conformal mapping for high genus surfaces with boundaries. *Comput. Graph.* **36**, 417–426 (2012).
42. Choi, G. Efficient conformal parameterization of multiply-connected surfaces using quasi-conformal theory. *J. Sci. Comput.* **87**, 70 (2021).
43. Falai, C. & Bert, J. Advances in geometric modeling and processing. *J. Molluscan Stud.* **76**, 404–406 (2010).
44. W. K. Sangawi, A., Murid, A. & Lee, K. W. Circular slit maps of multiply connected regions with application to brain image processing. *Bull. Malaysian Math. Sci. Soc.* **44** 171–202 (2020).
45. Sheffer, A. & de Sturler, E. Parameterization of faceted surfaces for meshing using angle-based flattening. *Eng. Comput.* **17**, 326–337 (2001).
46. Sheffer, A., Lévy, B., Mogilnitsky, M. & Bogomyakov, A. Abf++: fast and robust angle based flattening. *ACM Trans. Graph.* **24**, 311–330 (2005).
47. Lévy, B., Petitjean, S., Ray, N. & Maillot, J. Least squares conformal maps for automatic texture atlas generation. *ACM Trans. Graph.* **21**, 362–371 (2002).
48. Mullen, P., Tong, Y., Alliez, P. & Desbrun, M. Spectral conformal parameterization. *Comp. Graph. Forum* **27**, 1487–1494 (2008).
49. Botsch, M., Kobbelt, L., Pauly, M., Alliez, P. & Levy, B. Polygon mesh processing (A. K. Peters, 2010).
50. Gu, X., Luo, F. & Yau, S.-T. Computational conformal geometry behind modern technologies. *Not. Am. Math. Soc.* **67**, 1 (2020).

Author contributions

X.Z. and T.D. conceived the idea. X.Z., H.D., X.G., and T.D. designed the methodology. X.Z., H.D., and X.G. contributed equally to simulation, investigation and results visualization. X.M. and T.D. supervised the project. All authors contributed to the writing, review, and editing of the article.

Competing interests

The authors declare no competing interests.

Additional information

Supplementary information The online version contains supplementary material available at https://doi.org/10.1038/s42005-023-01322-w.

Correspondence and requests for materials should be addressed to Tianyu Dong.

Peer review information *Communications Physics* thanks Martin McCall and the other, anonymous, reviewer(s) for their contribution to the peer review of this work.

Reprints and permission information is available at http://www.nature.com/reprints

Publisher's note Springer Nature remains neutral with regard to jurisdictional claims in published maps and institutional affiliations.